

# Directly correlated microscopy of trench defects in InGaN quantum wells.

*T. J. O'Hanlon, F. C-P. Massabuau, A. Bao, M. J. Kappers & R. A. Oliver*

Department of Materials Science and Metallurgy, University of Cambridge, 27 Charles Babbage Road, Cambridge CB3 0FS, UK

## Abstract

Directly correlated measurements of the surface morphology, light emission and subsurface structure and composition were carried out on the exact same nanoscale trench defects in InGaN quantum well (QW) structures. Multiple scanning probe, scanning electron and transmission electron microscopy techniques were used to explain the origin of their unusual emission behaviour and the relationship between surface morphology and cathodoluminescence (CL) redshift. Trench defects comprise of an open trench partially or fully enclosing material in InGaN QWs with different CL emission properties to their surroundings. The CL redshift was shown to typically vary with the width of the trench and the prominence of the material enclosed by the trench above its surroundings. Three defects, encompassing typical and atypical features, were prepared into lamellae for transmission electron microscopy (TEM). A cross marker technique was used in the focused ion beam-scanning electron microscope (FIB-SEM) to centre the previously characterised defects in each lamella for further analysis. The defects with wider trenches and strong redshifts in CL emission had their initiating basal-plane stacking fault (BSF) towards the bottom of the QW stack, while the BSF formed near the top of the QW stack for a defect with a narrow trench and minimal redshift. The raised-centre, prominent defect showed a slight increase in QW thickness moving up the QW stack while QW widths in the level-centred defect remained broadly constant. The indium content of the enclosed QWs increased above the BSF positions up to a maximum, with an increase of approximately 4% relative to the surroundings seen for one defect examined. Gross fluctuations in QW width (GWWFs) were present in the surrounding material in this sample but were not seen in QWs enclosed by the defect volumes. These GWWFs have been linked with indium loss from surface step edges two or more monolayers high, and many surface step edges appear pinned by the open trenches, suggesting another reason for the higher indium content seen in QWs enclosed by trench defects.

## Introduction

With a bandgap spanning the entire visible range, quantum well (QW) structures based on  $\text{In}_x\text{Ga}_{1-x}\text{N}$  (usually shortened to InGaN) are the key component in a broad range of optoelectronic devices<sup>1-6</sup>. Despite their widespread use in efficient devices, heteroepitaxial growth of these devices (on sapphire, silicon or SiC substrates) still results in high levels of extended defects. The most prevalent of these are threading dislocations originating in the GaN pseudo-substrate<sup>7</sup>, which tend to open up into hexagonal pits called 'V-defects' upon intersecting the InGaN QWs. V-defects have been explored extensively<sup>8,9</sup> but other volume defects in InGaN QWs can have a significant effect on the emission behaviour. One example is the so called 'trench defect', which displays a complex relationship between its morphology and emission characteristics. Despite early studies suggesting these were inclusions within a V-defect<sup>10,11</sup>, they have a distinct structure; these defects initiate in the QW stack with a basal plane stacking fault (BSF), with the resulting vertical stacking mismatch boundary (SMB) separating the enclosed QWs in the faulted material from the surrounding QWs<sup>12</sup>.

Further up the QW stack, this boundary opens up as hexagonal pits where it changes direction, and these pits coalesce to form a trench encircling a central region with differing emission characteristics to the surroundings. Although initial experiments on multiple quantum well (MQW) structures suggested that trench defects may enclose a region of enhanced emission, research on full LED structures including an annealed p-cap indicates that the presence of trench defects can significantly reduce device efficiency. This is particularly relevant to the optimisation of green LEDs, since trenches are particularly prevalent in green-emitting InGaN material grown at reduced temperatures, with their density increasing by 2 orders of magnitude across a 90°C decrease in the InGaN growth temperature<sup>13</sup>.

Various strategies have been adopted to reduce the density of these defects<sup>10,11,14–16</sup>, most notably by suppressing BSF formation with H<sub>2</sub> gas during the growth of the GaN barriers, and by increasing the InGaN growth temperature. However, these techniques are all harder to implement in green-emitting material; H<sub>2</sub> reduces indium incorporation<sup>17</sup> and, even if H<sub>2</sub> is only used for barrier growth, the resultant QWs are typically thinner on average and of lower indium content<sup>14</sup> (even when protected by a thin GaN capping layer<sup>18</sup>). Similarly, increasing the InGaN growth temperature reduces the indium incorporation<sup>19</sup> and the average well thickness<sup>20</sup>. The combination of the increase in trench defect density in green-emitting InGaN QWs and the increased difficulty in removing them suggests a greater understanding of these complex defects may help in addressing the so called 'green gap' of reduced efficiency in longer wavelength emitting devices.

Previous directly correlative work identified two main factors of the trench defects' surface morphology (characterised by atomic force microscopy (AFM)) which affected the wavelength and intensity of their emission in scanning electron microscopy cathodoluminescence (SEM-CL). These were the thickness of the bounding trench and the prominence of the enclosed material (i.e. its height relative to the surroundings, where a positive prominence implies the defect enclosed region protrudes up above the surrounding undefected surface)<sup>21</sup>. Emission from QWs in the enclosed region was usually redshifted relative to emission from the surrounding QWs, though a blueshift in emission has also been seen under certain growth conditions<sup>22</sup>. Increasing trench thickness firmly correlated with an increase in this relative redshift, and the intensity of the emission relative to the surroundings also increased. The relationship of the redshift with prominence was less clear; large relative redshifts were likely to correlate with an increased prominence, but many level- and lowered-centre trench defects also showed a clear redshift in emission, suggesting that an increase in QW width in the enclosed material was an unlikely source of the redshift. Instead, it was posited that the enclosed InGaN QWs may have a higher indium fraction, though the reduction in emission intensity (via the quantum-confined Stark effect<sup>23</sup>) expected in strained indium-rich QWs was not observed.

In this work, the origin of the shift in CL emission wavelength is explored using a multi-microscopy approach, combining multiple imaging techniques in sequence on the same specific defects. By identifying the relationship between local CL redshift and surface morphology for a population of trench defects (by correlated AFM and SEM-CL), individual defects could be classified as having high or low values of trench thickness, prominence and/or redshift. Specific, representative trench defects were then selected, isolated and extracted by focused ion beam-scanning electron microscopy (FIB-SEM). Further conventional and scanning transmission electron microscopy (TEM and STEM) imaging and energy dispersive X-ray spectroscopy (EDX) analysis on the chosen defects could then be compared to their morphology and emission characteristics to help explain trench defects' unusual emission behaviour.

## Experimental Methods

The trench defects studied here were present on a 10-period InGaN / GaN QW structure grown by metal-organic vapour phase epitaxy (MOVPE) in a Thomas Swan 6 × 2 inch close-coupled showerhead reactor operating at 300 Torr. The same sample has previously been studied by Massabuau *et al.*<sup>21</sup> C-plane sapphire with a miscut of  $(0.25 \pm 0.10)^\circ$  towards  $(11\bar{2}0)$  was used as the substrate, on which a 30 nm thick GaN nucleation layer was first deposited at 540°C, followed by approximately 5 μm of GaN grown at 1020°C to act as a pseudo-substrate. On this pseudo-substrate, each InGaN QW was grown at 745°C for 216 s, followed by 2 s of GaN deposition at the same temperature, after which (as the GaN growth continued) the temperature was steadily increased to 860°C over a 94 s period, where it was held until about the GaN barrier was about 7.5 nm thick. (This growth method has previously been referred to as a ~Q2T method, distinguished from a quasi-two-temperature (Q2T) method by the shorter duration of the barrier growth carried out at the QW growth temperature<sup>24</sup>.) This cycle was repeated to form a 10-period structure. Trimethylgallium, trimethylindium and ammonia were used as precursor sources of gallium, indium and nitrogen, with H<sub>2</sub> as the carrier gas for GaN growth and N<sub>2</sub> used for InGaN growth. X-ray diffraction measurements on this sample gave  $(2.2 \pm 0.1)$  nm thick In<sub>x</sub>Ga<sub>1-x</sub>N QWs with  $x = 0.175 \pm 0.01$ , and a GaN barrier thickness of  $(7.5 \pm 0.1)$  nm, using the method of Vickers *et al.*<sup>25</sup>

Narrow bar 300 mesh TEM grids (Agar Ref: AGG2740C) were fixed to the wafer surface using thermal wax and used as finder grids to locate the same trench defects in AFM, SEM-CL and FIB-SEM. AFM measurements were performed in intermittent contact / tapping mode on a Veeco Dimension 3100 and the data analysed with the open-source Gwyddion software package<sup>26</sup>. SEM-CL was carried out at room temperature on a Philips XL30 FEG SEM operating at 5 kV with a Gatan MonoCL4 cathodoluminescence system using the charge coupled device camera. A grating spacing of 300 lines/mm and entry slit size of 0.2 mm was used, giving an approximate bandpass of 3 nm. To ensure consistency with the earlier correlative results of Massabuau *et al.*<sup>21</sup>, similar methods were used to calculate the thickness of the surrounding trench, the enclosed material's prominence, and the redshift and intensity of CL emission for each defect. The prominence and trench thickness values for each defect were calculated from line profiles oriented along the fast scan direction and positioned so the left-hand edges of the trenches were perpendicular to the line profiles. Figure 1 summarises how the prominence and trench thickness were measured from a line profile. Plane levelling was performed for each defect to level the surface step terraces (giving a staircase appearance) and the trench thickness was measured 2 nm below the higher adjoining terrace of the surrounding material (which varies less with the change in AFM tip radius than the full-width half-maximum (FWHM) or depth as a measure of trench size). In the rare instances where the enclosed material was more than 2 nm below the left-hand step edge, the trench sidewall profile was extended up to the 2 nm line and the extrapolated width was measured. The prominence was calculated as the difference between the height of the enclosed region and the average height of the surroundings to the left and right of the defect, i.e. as  $h_{\text{enclosed}} - (h_{\text{left}} + h_{\text{right}})/2$ , where  $h_i$  is the height of region  $i$ .

CL spectra were collected at each pixel of line scans through each trench defect, positioned so the middle third of the line intersected the trench defect. Monte Carlo simulations on this structure, using the CASINO software package<sup>27</sup>, suggest the interaction volume (the most important consideration for the CL generation volume in bulk 3d samples<sup>28</sup>) extends through the entire QW stack for a 5 keV beam. For trench defects where the BSF forms above the bottom of the QW stack,

a superposition of CL emission from QWs both enclosed by and below the defected volume would thus be recorded<sup>21</sup>. Hence, a two-Gaussian model was fitted to each spectrum by least-squares minimisation, giving two peaks of wavelength  $\lambda_1$  &  $\lambda_2$  and intensity  $I_1$  and  $I_2$ , with the overall wavelength,  $\lambda$ , at each point calculated as the intensity weighted mean of  $\lambda_1$  &  $\lambda_2$ . The resultant redshift of each defect was then defined as  $\lambda_{\text{enclosed}} - \lambda_{\text{surroundings}}$ , and the intensity ratio was defined as,  $(I_1 + I_2)_{\text{enclosed}} / (I_1 + I_2)_{\text{surroundings}}$ , consistent with the analysis of Massabuau *et al.*<sup>21</sup>

Specific trench defects were prepared as TEM lamellae for further analysis using an FEI (now Thermo Fisher Scientific) Helios NanoLab FIB-SEM. The standard in situ lift-out process<sup>29</sup> was modified to ensure the chosen defects could be located throughout the lamellae thinning and to ensure they were centred in each final sample. Full details of the approach are published separately<sup>30</sup>. Briefly, cross-shaped markers were deposited on top of each trench defect by electron beam-induced deposition prior to depositing the protective platinum strap. The cross arms were visible on the cross-sections of the lamellae throughout the entire thinning process, and the cross arms converged as each thinning face approached the trench defect location, ensuring each lamella bisected the chosen trench defect. The lamellae were thinned until there was none of the surrounding material in front or behind the enclosed QWs to avoid projection effects, and this method allowed trench defects down to less than 100 nm in diameter at the surface to be centred in the prepared lamellae. Lamellae were prepared with the thin direction parallel to the GaN  $[11\bar{2}0]$  direction and were finished with a low energy FIB polish with a 5 keV beam.

Diffraction contrast TEM, high-angle annular dark-field STEM imaging (STEM-HAADF) and STEM-EDX were performed on each lamella with an FEI (now Thermo Fisher Scientific) Tecnai Osiris S/TEM operating at 200 keV. The HAADF detector had a semi-angle from 65.3 mrad to 200 mrad, resulting in STEM-HAADF images with composition-dependent contrast. The EDX spectral components were separated by non-negative matrix factorisation and the gallium and indium contents were quantified by the Cliff-Lorimer  $k$ -factor method<sup>31</sup>. Composition profiles were obtained by taking a line scan across the QW stacks and averaged over the width of the line scan, giving a typical error of *ca.* 0.5% (and *ca.* 1% for trench B). To limit beam-induced damage during the TEM experiments<sup>32,33</sup>, TEM alignments were conducted outside each region of interest, only illuminating the region of interest during the measurements and keeping the exposure duration to a minimum.

## Results & discussion

### Correlated AFM and SEM-CL

For the first stage of the correlated multi-microscopy analysis, AFM and SEM-CL measurements were performed on the same 84 trench defects. An example of correlated imaging of these trench defects is shown in Figure 2, with the change in the emission intensity of the enclosed material seen in the panchromatic CL in (b). For approximately 95% of the trench defects, the emission from the enclosed material exhibits a redshift relative to the surrounding material (and the slight blueshift recorded for the remainder was similar in value to the spectral resolution). The trench topographical parameters previously identified to affect the emission were the trench thickness and the prominence of the enclosed region, and these are plotted against the redshift and intensity ratio for each trench defect in Figure 3. The observed trends agreed with our expectations based on the previous analysis of Massabuau *et al.*<sup>21</sup> A firm positive correlation between the thickness of the surrounding trench and both the redshift and logarithmic intensity ratio was seen in subfigures (a) and (b), with coefficients of determination,  $R^2$ , of 0.62 and 0.52 respectively. As expected, the relationship of the redshift to

prominence shown in subfigure (c) was less clear cut, with a weak positive correlation ( $R^2 = 0.36$ ). If a trench defect had a high prominence, its emission was likely to be redshifted, but large redshifts were also seen for low and slightly negative prominence values. For the intensity ratio in (d), a clear relationship with prominence was neither expected nor observed.

### Selection of defects for detailed analysis in STEM-HAADF

Having established the range of variation in morphological and emission characteristics across the population, and identified the expected trends between them, specific trench defects could then be chosen for further analysis to help explain the relationship between trench morphology and the redshifted emission. Two potential causes for this redshift were previously suggested: a possible increase in the indium content of the enclosed InGaN QWs or a possible increase in the QW thickness, both relative to the surroundings. To separate these two effects, three trenches were chosen from across the distributions, indicated as 'A', 'B' and 'C' in Figure 3. AFM height images and CL spectra for A, B and C are shown in Figure 4. Trench defect A had a low prominence value, a small trench thickness and a low redshift. B also had a low prominence, but had a large trench thickness and large redshift value. Finally, C was chosen with a high redshift value close to that of defect B, but with a high prominence, which gave a trench of intermediate thickness. The relevant parameters are given in table 1. Errors in the trench thickness values are nominally  $\pm 8$  nm, given by the tip half-width and the pixel spacing. The AFM's noise floor of  $\pm 0.03$  nm gives the nominal uncertainty in the prominence values and the bandpass for the redshift measurements for the CL setup was approximately 3 nm.

Table 1: Morphological and emission metrics of the trench defects chosen for further investigation.

Trench Defect	Thickness (nm) $\pm 8$ nm	Prominence (nm) $\pm 0.03$ nm	Redshift (nm) $\pm 3$ nm	Intensity Ratio
A	25	0.02	1.5	0.5
B	80	0.17	19	2.0
C	52	8.40	19	0.95

### STEM-HAADF imaging of the selected defects previously studied in AFM and SEM-CL

TEM lamellae were prepared bisecting each of these trench defects by FIB-SEM using the cross marker method described in the Methods section. Figure 5 shows the cross-sections of trench defects A, B and C imaged by STEM-HAADF and by dark field (DF) TEM with  $g = 1\bar{1}00$ . (Subfigures (c) and (f) were included in a separate *Ultramicroscopy* publication to demonstrate the efficacy of the cross marker lift out method developed to prepare these directly correlated samples<sup>30</sup>.) The surrounding trenches for B and C are much wider and deeper than in A. The dark contrast of the bounding BSF and SMBs are seen in Figure 5(d)-(f). The BSFs in defects B and C with wide trenches are found at the first and second QWs to be grown respectively, whereas the BSF in defect A did not form until the ninth QW. For this defect with a narrow bounding trench, most of the wells in the QW stack probed by SEM-CL at the defect location are not contained in the defected volume, so the emission is similar to the surroundings. In B and C however, most of the QWs are contained in the defect volume, partly explaining the greater divergence in emission behaviour from that of the surrounding material. We note that Massabuau *et al.*<sup>21</sup> postulated two explanations for the observation of low intensity ratios for narrow trenches: either (1) the BSF was formed early in the QW stack, but the trench failed to open, leading to an extended SMB which acted as a non-radiative

recombination centre for carriers injected into the enclosed volume or (2) the BSF was formed late in the QW stack, and the majority of the emission did not arise from within the trench, whilst such carriers as were injected into the trench were susceptible to non-radiative recombination at the BSF. Our data on trench defects A, B and C strongly support the latter explanation.

Fluctuations in the width of the QWs can be seen in the material surrounding the trench. Such gross well-width fluctuations (GWWFs) where the thickness and continuity of the QWs varies laterally are known<sup>34</sup> to result from the InGaN/GaN QW growth method used here. However, the QWs enclosed by the trench defects above the BSF appeared free of GWWFs, at least in the portion of the enclosed QWs intersected by the TEM lamellae. The difference in QW smoothness inside and outside the defect can be seen more clearly in the inset to Figure 5(c). In addition, much thinner QWs are visible on the trench sidewalls similar to those seen for V-defects<sup>9</sup>, which may have an important role in shielding carriers from the non-radiative SMBs<sup>21</sup>. Though these QWs have been discussed previously, we believe this investigation provides the first direct images of these sidewall QWs in InGaN trench defects.

### **STEM-EDX measurements on the selected defects**

STEM-EDX profiles for the atomic fraction of indium through the QW stack are shown in Figure 6, with the growth direction being from right to left. The EDX profiles taken from the surrounding material adjacent to the trench defects (with the trace outside C shown in Figure 6(d)) showed a fairly consistent indium content in all QWs in the stack, notwithstanding the variation caused by the GWWFs. The profile for the QWs in trench defect A is similar to those for the surroundings; this is unsurprising given the BSF did not form until the penultimate QW, so most of the QWs are not contained in the defect volume. Inside B & C, however, the indium fraction begins to increase in QWs grown above the BSF position, up to a maximum for wells 7 to 10. For B & C, QWs 7 to 10 are adjacent to the open trench (though as growth also proceeds on the trench sidewalls, some of the lower QWs would have formed next to open trenches which were subsequently filled in). This increase is most clearly seen when comparing Figure 6(c) and (d). A lower pixel density was used for the data in Figure 6(b) (which was necessary to reduce the effects of sample drift on this sample) giving a slight reduction in the measured indium content inside and outside the trench defect (due to overlap with the GaN QBs). Nevertheless, an increase in indium content of the enclosed QWs is observable in this case too.

By comparing subfigures (c) and (d) in Figure 6, there appears to be an increase of approximately 4% in the indium content of the uppermost QWs in trench C compared to the surrounding material, with a similar level of increase seen for B. Although part of this measured increase could relate to the lack of GWWFs in the enclosed QWs, relative to the surroundings, the continued increase in indium content above the BSF (see QWs 3 to 7 in Figure 6(c)) suggests the enclosed wells do indeed contain a higher indium fraction than the surroundings. The overlap of the interaction volume with the GaN barriers during STEM-EDX analysis, coupled with inevitable gallium implantation during the FIB preparation of the lamellae, gave an underestimate of the overall indium content of these samples. X-ray diffraction measurements across the wafer suggest that the average indium fraction,  $x$ , in the quantum wells is  $0.175 \pm 0.01$ . The maximum indium fraction seen here may then be closer to 0.21 – 0.22, but the relative increase still applies.

## Quantum well width measurements on the selected defects

QW widths inside and outside the defects were determined from QW FWHM in the STEM-HAADF data, with the distances calibrated using the QW period spacing across the wafer measured by X-ray diffraction. The GWWFs in the surrounding material made capturing accurate well widths challenging, although efforts were made to avoid the most severe GWWFs. Nonetheless, the observed thicknesses will have a dependence on whether the final TEM lamella intersected a more or less fluctuating region.

The QW widths for defect A were similar inside and outside the trench, fluctuating with the GWWFs outside the enclosed trench volume but showing no clear trend. The enclosed QWs in B had similar widths throughout the QW stack, but did appear slightly thicker than the surrounding QWs due to the absence of visible GWWFs in the enclosed wells, despite the fact that the enclosed material was not raised above the surrounding material (near zero prominence). The maxima of the QW widths inside and outside the defect region were more similar, however, and as carriers would be expected to recombine at these thicker, lower band gap locations in the surrounding wells, the redshift would not be expected to follow the difference in *average* QW widths in these samples with fluctuating well thicknesses.

The QW widths for C, which had a high prominence compared to the rest of the trench defect population, are shown in Figure 7. The error bars show the standard error for each width value. Though the second QW appears artificially wide due to overlapping contrast from the BSF, the enclosed QWs do appear to be slowly increasing in width as they get closer to the surface when compared to the fluctuating but stable QWs in the surroundings. The difference between the width of the enclosed QWs and those in the surroundings reaches a maximum of approximately 0.5 nm for the tenth QW, and the GaN barriers between the final 4 QWs were also noticeably wider, in line with the high prominence value of defect C. The overall redshift measured is influenced by emission from each QW beneath the electron beam, however, so the resultant redshift value would be smaller than if all the QWs had this increase in width. This gradual increase may also explain the wider FWHM of the CL emission from the enclosed wells for C in Figure 4. Defects B and C have similar redshift values, but the final QWs in C were wider while the QW thickness throughout B was fairly constant. This difference may be offset by the wider trench and lower BSF in B, so the indium fraction increase may be greater for B than C, accounting for their similar redshift values, but the less precise data in Figure 6(b) is not clear enough to confirm this directly.

## Simulations and discussion

A number of simulations of a simple InGaN/GaN single QW structure with indium fractions of 0.16 – 0.22 and QW widths of 2.1 to 3.1 nm were carried out, using a self-consistent Schrödinger-Poisson calculation at 300K in the nextnano™ software package<sup>35</sup>. The calculated shift in emission wavelength (for transitions from the conduction band to heavy hole band) for a 4% indium increase ranged from 30 nm (for narrow wells) to 50 nm (for wide wells), with 2.5 nm QWs showing a 31 – 39 nm redshift for a 4% increase. Increases of 0.5 nm in the QW width gave redshifts of 20 – 35 nm. These values lead to an overestimate of the CL redshift values observed for trench defects B and C. However, the simulated values were only calculated for a single QW structure. The full QW stack is expected to influence the measured CL emission and only the QWs nearest the surface have the highest indium composition (and width in C). Although QWs at different depths will contribute different proportions of the total emission to the recorded intensity<sup>36</sup>, overall, the variation in QW properties through the stack will reduce the measured redshift relative to that expected for the QW nearest to the surface. Another important consideration is the impact of possible elastic strain relaxation at the open trenches (discussed below) which would reduce the overall redshift by lessening the impact of the quantum-confined Stark effect in the QWs<sup>37,38</sup>, which was not represented in the model.

For these trench defects, the correlated AFM and SEM-CL data demonstrated the relationship between trench thickness and CL emission redshift. This redshift in emission from the enclosed material was shown to match with an increased indium fraction in the QWs for the three defects examined in detail in the TEM, with the increase beginning above the BSF before slowing to a maximum adjacent to the open trench. The two possible routes for an increase in the enclosed QWs indium content previously postulated by Massabuau *et al.* were strain relaxation in the enclosed material and selective area epitaxy (SAE) effects when considering the trench as a mask<sup>21</sup>. Briefly, for a strain relaxation mechanism, the formation of the bounding trench (and BSF / SMB formation) may reduce the compressive strain in the enclosed QWs<sup>39,40</sup>. This would allow a greater incorporation of indium, with its larger InN bond length, via the compositional pulling effect<sup>41</sup>. Regarding SAE, Shioda *et al.* showed emission wavelengths from near-mask-edge regions of SAE-grown InGaN were longer for wider mask widths. However, their masks were 10s of  $\mu\text{m}$  wide<sup>42</sup>, so these diffusion-controlled effects may not apply on the significantly smaller length scales masked by the open trenches.

In the samples investigated here, the absence of GWWFs in the enclosed QWs may suggest another possible mechanism for increased indium content, when considered in tandem with the AFM data. Jouvot *et al.* showed that the spacing and orientation of elongated troughs in an annealed InGaN epilayer matched with the spacing and orientation of double-monolayer surface steps on the underlying GaN pseudo-substrate, and hence attributed the formation of GWWFs to preferential desorption of material in the vicinity of double height steps. In addition, local changes in emission wavelength have been observed in the vicinity of bunched macrosteps in InGaN QW samples<sup>43</sup> and InGaN layers<sup>44</sup>. In the AFM height maps of the sample surface the terrace step edges were kinked around the trench defects, as shown in Figure 2(a), possibly having been pinned at the open trenches. Consequently, the enclosed surfaces appeared smoother than those surrounding the defects. For trench defects A, B and C, any changes in step height on the surface enclosed by the trenches are single-monolayer steps (i.e. half the unit cell height), whereas the bunching of the steps on the surface surrounding the defects gives many double or multiple-monolayer height changes.

If the different bonding environment at these taller step edges makes them more susceptible to the loss of indium during the GaN barrier growth, their absence on the enclosed surface of these trench defects may contribute to both a reduced density of GWWFs and an increase in the indium content of the enclosed QWs for samples grown by the  $\sim$ Q2T method, or where a temperature ramp is carried out without any protective GaN cap. However, it should be noted that this mechanism would explain the existence of higher indium contents in general within the enclosed region, but would not explain the gradual increase in indium content up the QW stack. Furthermore, trench defects in InGaN/GaN samples grown with low temperature QBs or with thicker low temperature GaN capping layers prior to high temperature QB growth also display altered emission properties relative to their surroundings, so it would be instructive to examine these separately, as comparisons may reveal the extent to which this alteration in GWWF formation affects the indium incorporation inside these surprisingly complex defects.

## Conclusions

Directly correlated microscopy by sequential AFM, SEM-CL and TEM-based imaging and analysis was performed on three trench defects, selected from specific parts of the defect population in relation to their surface morphology and CL emission characteristics. Defects with wide bounding trenches and strong redshifts were seen to have their initiating BSF close to the bottom for the QW stack, whereas the BSF formed later, towards the top of the stack for the narrow-trenched defect. Consequently, for wider bounding trenches, a higher proportion of the QWs probed by CL would be enclosed by the defect volume when compared to a narrower trench feature. For the trench defects

with low BSFs, QW widths remained fairly constant in the non-prominent trench defect while the prominent-centre trench defect showed a slight increase in well widths moving up the QW stack.

The indium content of the enclosed QWs was seen by STEM-EDX to increase above the BSF position, and to continue to increase inside the defect volume until reaching a plateau, with the maximum for trench defect C approximately 4% higher in indium fraction than the surrounding QWs. This increase may be linked to strain relaxation effects (or possible nanoscale SAE) arising from the open trenches, but may also be linked to differences in the smoothness of the enclosed QWs; GWWFs observed across the sample were not visible in QWs enclosed in the defect volumes. GWWFs have been linked with the loss of indium from surface step edges two or more monolayers in height, and many surface step edges appear to be pinned at the open trenches as seen in AFM. Step height changes of multiple monolayers were seen in the surrounding material, but only monolayer changes in height were seen in the enclosed surfaces of A, B and C. For samples exhibiting GWWFs, their absence in QWs enclosed by the defects may offer an additional mechanism for the increase in QW indium content (and concurrent redshift in emission) relative to the surrounding material.

## Acknowledgements

This work was supported by the European Research Council under the European Community's Seventh Framework Programme (FP7/2007–2013)/ERC Grant Agreement No. 279361 (MACONS) and by EPSRC (Grant No. EP/M010589/1). The authors would like to thank Siyuan Zhang and Wai Yuen Fu for sharing their EDX analysis scripts.

## Figures

Figure 1

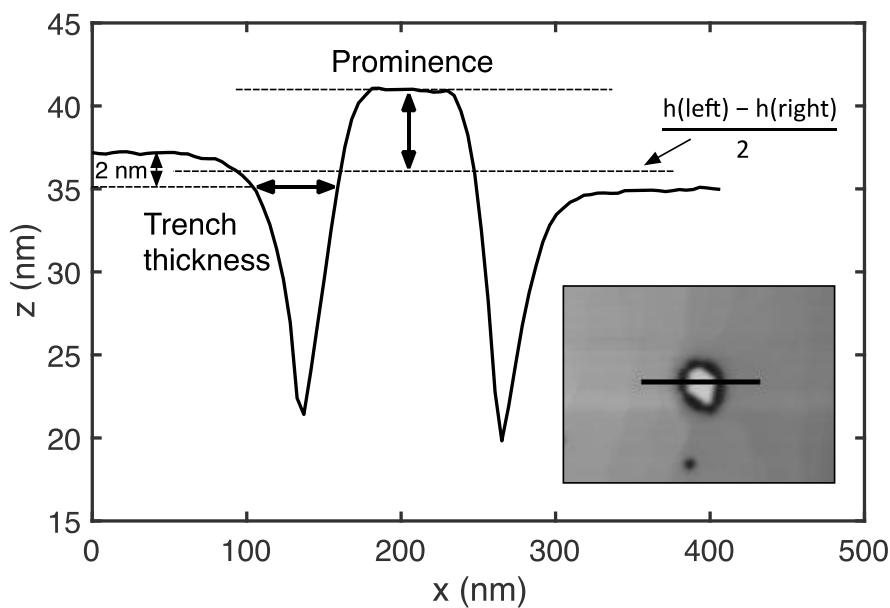


Figure 1: Line profile through a trench defect showing how the prominence and trench thickness were calculated. Inset: AFM height image of the trench defect showing the profile position. The small feature at the bottom of the inset is a V-defect.

Figure 2

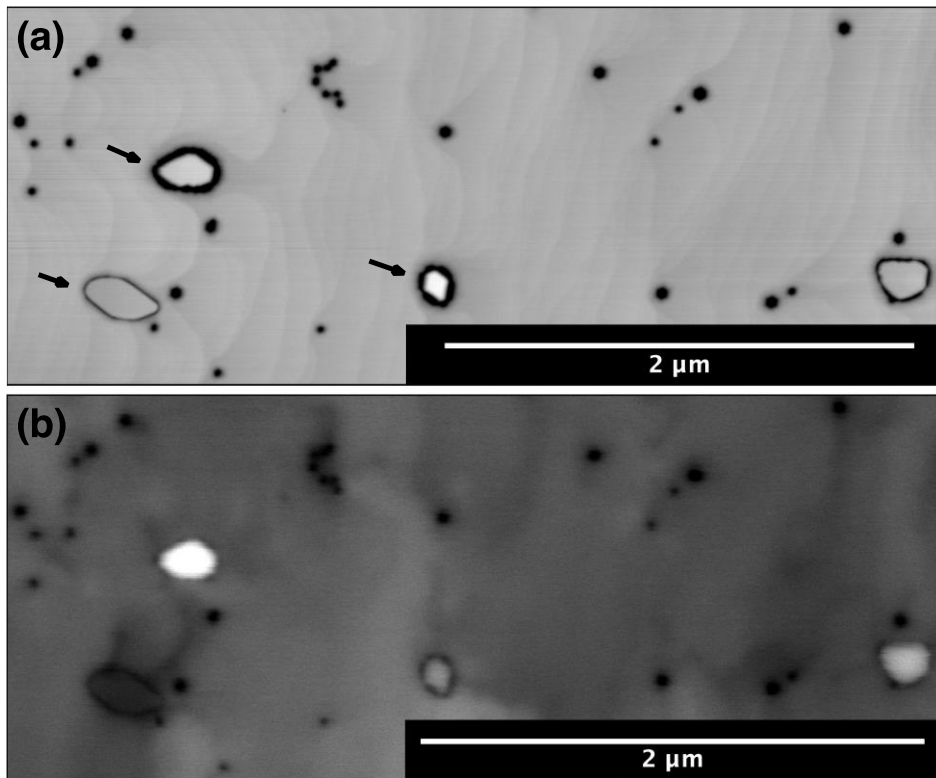


Figure 2: The same trench defects seen in AFM (a) and panchromatic CL (b), with small hexagonal V-defects also visible. The height range in (a) was set to 16.1 nm to reveal the surface step edges, which appear pinned by the open trenches (as indicated by the arrows).

**Figure 3**

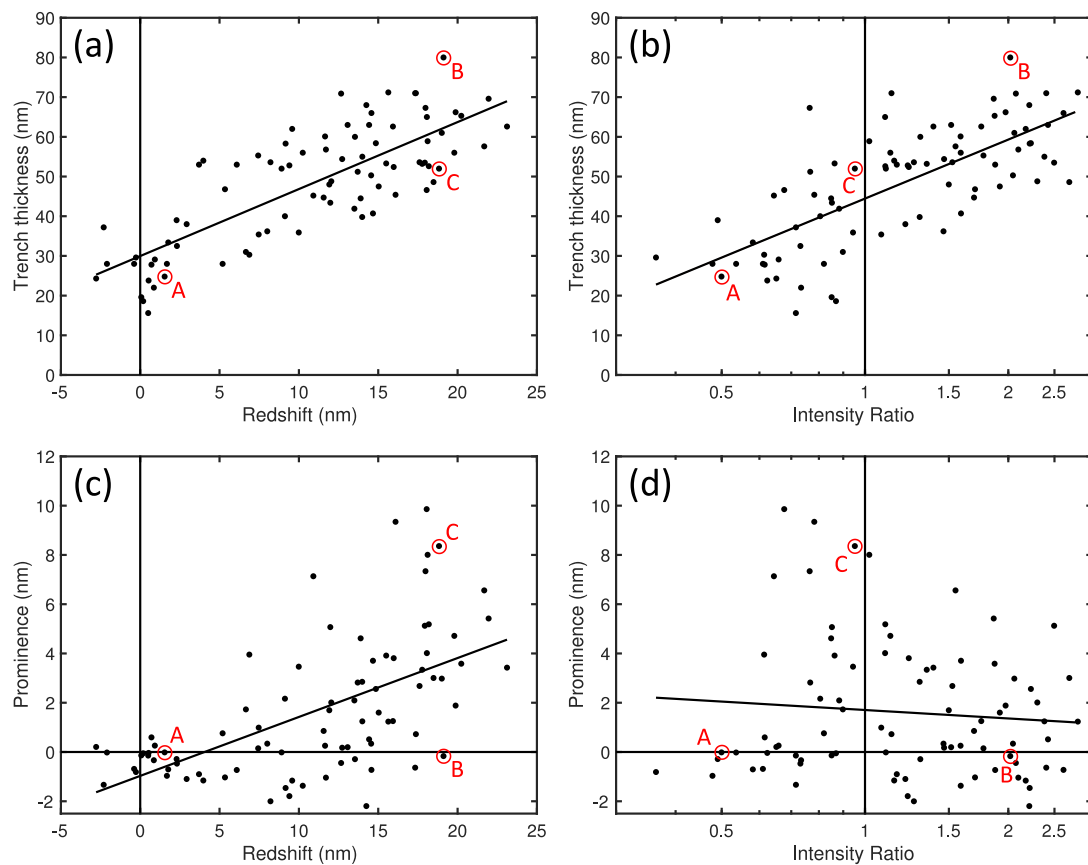


Figure 3: Scatter plots for the population of trench defects showing how the trench thickness influences the redshift (a) and intensity ratio (b) of the CL emission, and how the measured prominence influences the redshift (c) and intensity ratio (d) values. Lines of best fit are shown (nominally for (d)) with coefficients of determination,  $R^2$ , of 0.62, 0.52, 0.36 and  $< 0.01$  from (a) to (d) respectively.

**Figure 4**

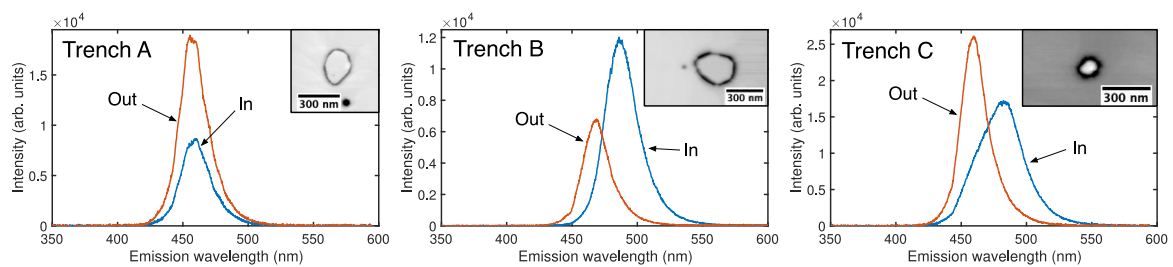


Figure 4: CL spectra recorded inside and outside trench defects A, B and C, showing the change in emission wavelength and intensity. The inset figures show AFM topography images of the defects with image heights of 18.1, 32.1 and 22.2 nm for A, B and C respectively. The FWHM of the spectrum recorded inside trench C is noticeably wider than for the other spectra.

Figure 5

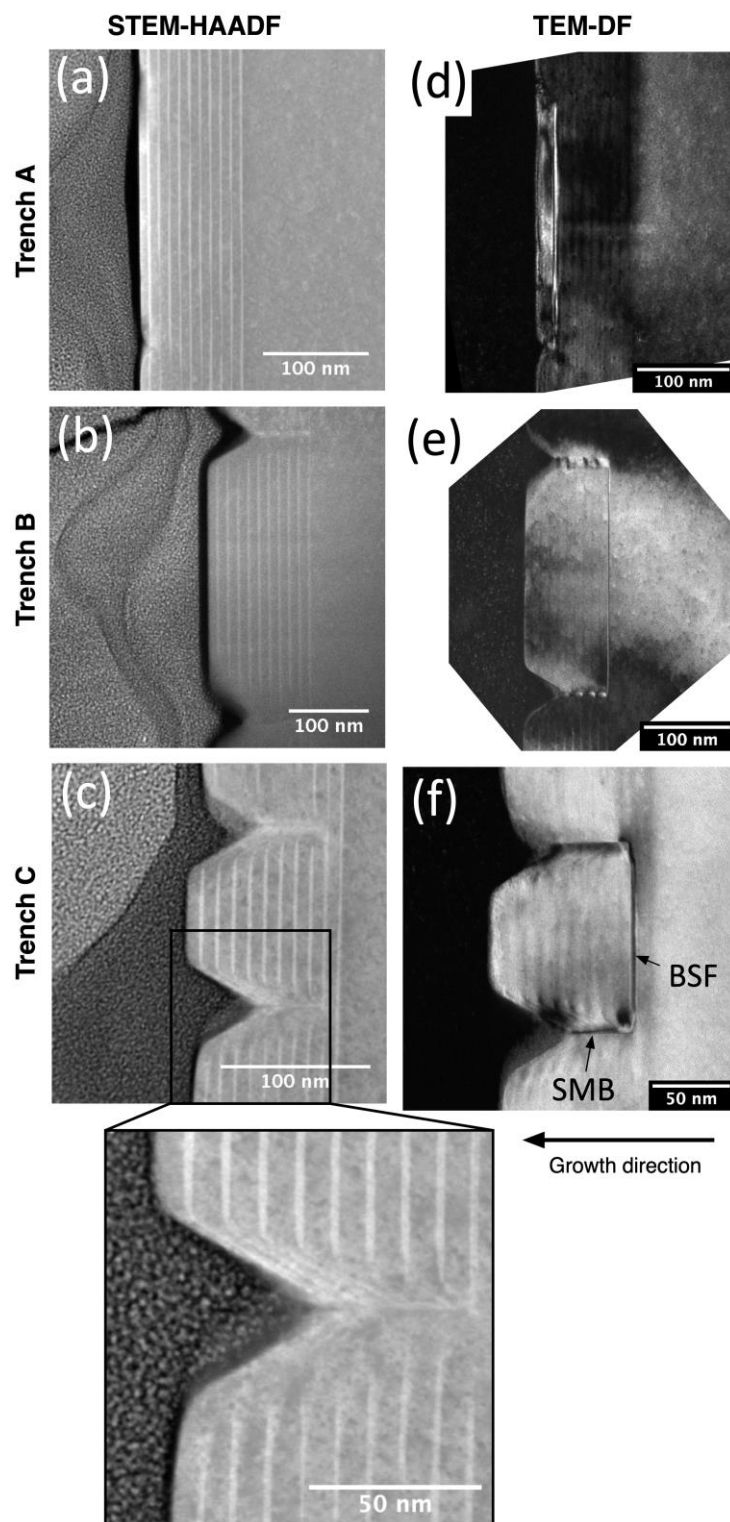


Figure 5: Cross-sectional STEM-HAADF images of trench defects A (a), B (b) and C (c), with the InGaN QWs seen as bright features and the trenches clearly visible. The inset in (c) shows the difference in QW smoothness inside and outside the defect region, and also shows the thin QWs on the trench sidewalls. DF TEM images of defects A (d), B (e) and C (f) taken with  $g = 1\bar{1}00$ , and show the BSF and SMB positions in the QW stack as indicated in (f). Protective platinum from the FIB preparation is on the left-hand side of the images, and the growth direction is right to left. Images were taken close to a  $\langle 11\bar{2}0 \rangle$ -type zone axis. Note: subfigures (c) and (f) were included in a separate Ultramicroscopy publication detailing the development of the cross marker lift out method used here<sup>30</sup>.

Figure 6

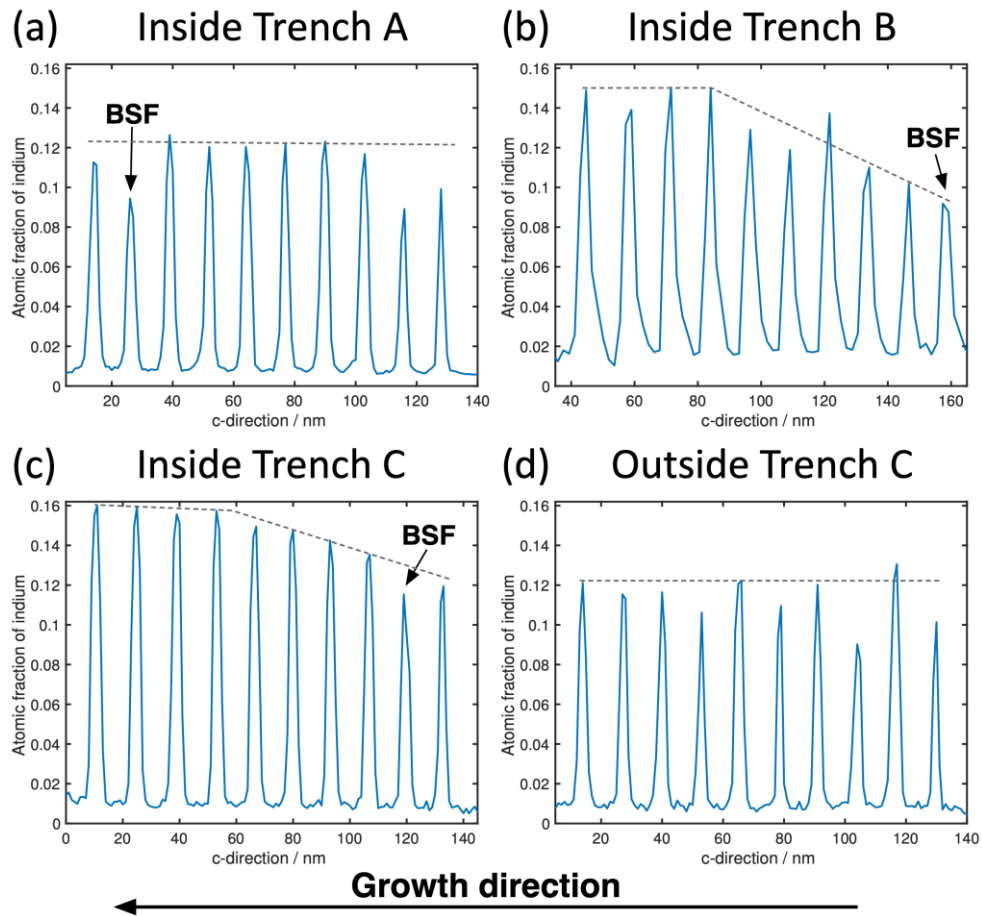


Figure 6: STEM-EDX profiles showing the variation in the atomic fraction of indium, taken from EDX maps across the QW stack, inside trench defect A (a), B (b) and C (c), and outside C (d). The BSF positions are marked for the enclosed QWs, and the last QW to form is on the left hand side in each case. Dashed lines illustrating the observed trends were added as guides to the eye.

**Figure 7**

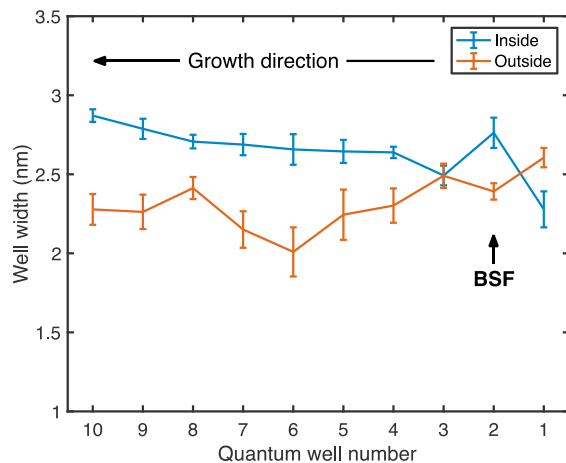


Figure 7: QW widths measured in STEM-HAADF inside and outside trench defect C, with QW 10 the last QW to form. The BSF position is indicated and the error bars show the standard error of the measurements.

## References

1. Hamaguchi, T., Tanaka, M. & Nakajima, H. A review on the latest progress of visible GaN-based VCSELs with lateral confinement by curved dielectric DBR reflector and boron ion implantation. *Jpn. J. Appl. Phys.* **58**, SC0806 (2019).
2. Wasisto, H. S., Prades, J. D., Gülink, J. & Waag, A. Beyond solid-state lighting: Miniaturization, hybrid integration, and applications of GaN nano- and micro-LEDs. *Appl. Phys. Rev.* **6**, 041315 (2019).
3. Weisbuch, C. Review—On The Search for Efficient Solid State Light Emitters: Past, Present, Future. *ECS J. Solid State Sci. Technol.* **9**, 016022 (2020).
4. Zhou, X. *et al.* Growth, transfer printing and colour conversion techniques towards full-colour micro-LED display. *Prog. Quantum Electron.* **71**, 100263 (2020).
5. Li, K. H., Fu, W. Y. & Choi, H. W. Chip-scale GaN integration. *Prog. Quantum Electron.* **70**, 100247 (2020).
6. Butté, R. & Grandjean, N. III-nitride photonic cavities. *Nanophotonics* **9**, 569–598 (2020).
7. Bennett, S. E. Dislocations and their reduction in GaN. *Mater. Sci. Technol.* **26**, 1017–1028 (2010).
8. Wu, X. H. *et al.* Structural origin of V-defects and correlation with localized excitonic centers in InGaN/GaN multiple quantum wells. *Appl. Phys. Lett.* **72**, 692 (1998).
9. Hangleiter, A. *et al.* Suppression of Nonradiative Recombination by V-Shaped Pits in GaInN / GaN Quantum Wells Produces a Large Increase in the Light Emission Efficiency. *Phys. Rev. Lett.* **95**, 127402 (2005).
10. Ting, S. M. *et al.* Morphological evolution of InGaN/GaN quantum-well heterostructures grown by metalorganic chemical vapor deposition. *J. Appl. Phys.* **94**, 1461 (2003).
11. Florescu, D. I. *et al.* Investigation of V-Defects and embedded inclusions in InGaN/GaN multiple quantum wells grown by metalorganic chemical vapor deposition on (0001)

- sapphire. *Appl. Phys. Lett.* **83**, 33–35 (2003).
12. Massabuau, F. C.-P. *et al.* Morphological, structural, and emission characterization of trench defects in InGaN/GaN quantum well structures. *Appl. Phys. Lett.* **101**, 212107 (2012).
  13. Massabuau, F. C.-P. *et al.* The impact of trench defects in InGaN/GaN light emitting diodes and implications for the “green gap” problem. *Appl. Phys. Lett.* **105**, 112110 (2014).
  14. Massabuau, F., Kappers, M., Humphreys, C. & Oliver, R. Mechanisms preventing trench defect formation in InGaN/GaN quantum well structures using hydrogen during GaN barrier growth. *Phys. status solidi* **254**, 1600666 (2017).
  15. Smalc-Koziorowska, J., Grzanka, E., Czernecki, R., Schiavon, D. & Leszczyński, M. Elimination of trench defects and V-pits from InGaN/GaN structures. *Appl. Phys. Lett.* **106**, 101905 (2015).
  16. Kumar, M. S. *et al.* Surface morphological studies of green InGaN/GaN multi-quantum wells grown by using MOCVD. *Mater. Chem. Phys.* **113**, 192–195 (2009).
  17. Koukitu, A., Taki, T., Takahashi, N. & Seki, H. Thermodynamic study on the role of hydrogen during the MOVPE growth of group III nitrides. *J. Cryst. Growth* **197**, 99–105 (1999).
  18. Hu, Y.-L. *et al.* Effect of quantum well cap layer thickness on the microstructure and performance of InGaN/GaN solar cells. *Appl. Phys. Lett.* **100**, 161101 (2012).
  19. Ou, J., Chen, W.-K., Lin, H.-C., Pan, Y.-C. & Lee, M.-C. An Elucidation of Solid Incorporation of InGaN Grown by Metalorganic Vapor Phase Epitaxy. *Jpn. J. Appl. Phys.* **37**, L633–L636 (1998).
  20. Oliver, R. A. *et al.* The impact of gross well width fluctuations on the efficiency of GaN-based light emitting diodes. *Appl. Phys. Lett.* **103**, 141114 (2013).
  21. Massabuau, F. C.-P. *et al.* Correlations between the morphology and emission properties of trench defects in InGaN/GaN quantum wells. *J. Appl. Phys.* **113**, 073505 (2013).
  22. Vaitkevičius, A. *et al.* Influence of quantum-confined Stark effect on optical properties within trench defects in InGaN quantum wells with different indium content. *J. Appl. Phys.* **115**, 213512 (2014).
  23. Miller, D. A. B. *et al.* Band-Edge Electroabsorption in Quantum Well Structures: The Quantum-Confined Stark Effect. *Phys. Rev. Lett.* **53**, 2173–2176 (1984).
  24. Massabuau, F. C.-P. *et al.* Investigation of unintentional indium incorporation into GaN barriers of InGaN/GaN quantum well structures. *Phys. status solidi* **252**, 928–935 (2015).
  25. Vickers, M. E. *et al.* Determination of the indium content and layer thicknesses in InGaN/GaN quantum wells by x-ray scattering. *J. Appl. Phys.* **94**, 1565 (2003).
  26. Nečas, D. & Klapetek, P. Gwyddion: an open-source software for SPM data analysis. *Open Phys.* **10**, (2012).
  27. Drouin, D. *et al.* CASINO V2.42—A Fast and Easy-to-use Modeling Tool for Scanning Electron Microscopy and Microanalysis Users. *Scanning* **29**, 92–101 (2007).
  28. Edwards, P. R. & Martin, R. W. Cathodoluminescence nano-characterization of semiconductors. *Semicond. Sci. Technol.* **26**, 064005 (2011).
  29. Schaffer, M., Schaffer, B. & Ramasse, Q. Sample preparation for atomic-resolution STEM at low voltages by FIB. *Ultramicroscopy* **114**, 62–71 (2012).
  30. O’Hanlon, T. J., Bao, A., Massabuau, F. C.-P., Kappers, M. J. & Oliver, R. A. Cross-shaped

- markers for the preparation of site-specific transmission electron microscopy lamellae using focused ion beam techniques. *Ultramicroscopy* **212**, 112970 (2020).
31. Cliff, G. & Lorimer, G. W. The quantitative analysis of thin specimens. *J. Microsc.* **103**, 203–207 (1975).
  32. Smeeton, T. M., Kappers, M. J., Barnard, J. S., Vickers, M. E. & Humphreys, C. J. Electron-beam-induced strain within InGaN quantum wells: False indium ‘cluster’ detection in the transmission electron microscope. *Appl. Phys. Lett.* **83**, 5419 (2003).
  33. Baloch, K. H., Johnston-Peck, A. C., Kisslinger, K., Stach, E. A. & Gradecak, S. Revisiting the ‘In-clustering’ question in InGaN through the use of aberration-corrected electron microscopy below the knock-on threshold. *Appl. Phys. Lett.* **102**, 191910 (2013).
  34. van der Laak, N. K., Oliver, R. a., Kappers, M. J. & Humphreys, C. J. Characterization of InGaN quantum wells with gross fluctuations in width. *J. Appl. Phys.* **102**, 013513 (2007).
  35. Birner, S. *et al.* nextnano: General Purpose 3-D Simulations. *IEEE Trans. Electron Devices* **54**, 2137–2142 (2007).
  36. Toth, M. & Phillips, M. R. Monte Carlo modeling of cathodoluminescence generation using electron energy loss curves. *Scanning* **20**, 425–432 (2006).
  37. Pereira, S. *et al.* Strain and composition distributions in wurtzite InGaN/GaN layers extracted from x-ray reciprocal space mapping. *Appl. Phys. Lett.* **80**, 3913–3915 (2002).
  38. de Sousa Pereira, S. M., O’Donnell, K. P. & da Costa Alves, E. J. Role of Nanoscale Strain Inhomogeneity on the Light Emission from InGaN Epilayers. *Adv. Funct. Mater.* **17**, 37–42 (2007).
  39. Song, T. L. Strain relaxation due to V-pit formation in  $\text{In}_x\text{Ga}_{1-x}\text{N}/\text{GaN}$  epilayers grown on sapphire. *J. Appl. Phys.* **98**, 084906 (2005).
  40. Cho, H. K. *et al.* Microstructural characterization of InGaN/GaN multiple quantum wells with high indium composition. *J. Cryst. Growth* **231**, 466–473 (2001).
  41. Pereira, S. *et al.* Compositional pulling effects in  $\text{In}_x\text{Ga}_{1-x}\text{N}/\text{GaN}$  layers: A combined depth-resolved cathodoluminescence and Rutherford backscattering/channeling study. *Phys. Rev. B* **64**, 205311 (2001).
  42. Shioda, T., Sugiyama, M., Shimogaki, Y. & Nakano, Y. Selectivity enhancement by hydrogen addition in selective area metal-organic vapor phase epitaxy of GaN and InGaN. *Phys. status solidi* **207**, 1375–1378 (2010).
  43. Lermer, T. *et al.* Interdependency of surface morphology and wavelength fluctuations of indium-rich InGaN/GaN quantum wells. *Phys. status solidi* **208**, 1199–1202 (2011).
  44. Kryśko, M. *et al.* Correlation between luminescence and compositional striations in InGaN layers grown on miscut GaN substrates. *Appl. Phys. Lett.* **91**, 1–4 (2007).